18 Visualization and Resolution in Localization Microscopy

Robert P.J. Nieuwenhuizen, Sjoerd Stallinga, and Bernd Rieger

CONTENTS

18.1 INTRODUCTION

Imaging beyond the diffraction limit via a set of techniques nowadays termed *localization microscopy* has seen a sharp rise after the initial works around 2006; the most notable methods introduced were (fluorescence) photoactivated localization microscopy (PALM)[1,2] and stochastic optical reconstruction microscopy.[3] The common idea to achieve imaging below the diffraction limit in the optical far field is to localize single stochastically activated fluorescent molecules. These molecules are

switched between a fluorescent on-state and a nonfluorescent off-state. The on-state molecules form a sparse subset of all molecules such that only one is active in a region the size on the order of the diffraction limit. The positions of these emitting molecules are estimated, after which they return to the off-state and other molecules are activated and localized until all molecules have been imaged. Essential to this process is the *localization* of single fluorescent molecules, hence the common name for the techniques. The high-resolution capability of these techniques follows from the precision with which the positions of the molecules can be estimated, which is much better than the diffraction limit.[4,5] This precision is on the order of $\sigma_{psf}/\sqrt{n}$, where n is the number of recorded emission photons and σ_{psf} is the width of the point spread function (PSF).[6,7] Typically, hundreds or thousands of photons can be recorded and with $\sigma_{psf} \approx 250$ nm, this results in commonly achieved localization precisions on the order of tens of nanometers, although smaller values in the range of nanometers have been reported.[8–10] In comparison, Abbe's diffraction limit is given by $\lambda/(2NA) \approx 200$ nm, where λ is the wavelength of light and NA is the numerical aperture of the imaging system. This superior precision is what makes localization microscopy images crisper and sharper than widefield images and explains the widespread use of the technique nowadays. Even now, more and more flavors of localization-based microscopy techniques are introduced; we give by no means an exhaustive list.[11–18]

18.2 RESOLUTION

As the family of localization microscopy techniques came of age and sharper and sharper images were recorded, the question "what is the resolution for these types of images?" arose. In other techniques for super-resolution imaging, such as stimulated emission depletion (STED) microscopy,[19,20] structured illumination microscopy (SIM),[21,22] or image scanning microscopy (ISM),[23,24] the system can be identified as having a smaller effective PSF. Once the width of this PSF is measured or calculated, the resolution in the Abbe sense can be given. Where Abbe and Nyquist defined resolution as the inverse of the spatial bandwidth of the imaging system,[25,26] Rayleigh and Sparrow captured resolution empirically. Rayleigh found a limit of $0.61\lambda/NA$ and Sparrow found a limit of $0.47\lambda/NA$, which is very similar to Abbe's diffraction limit of $0.5\lambda/NA$ for incoherent light. For localization microscopy, there is no natural extension of the PSF methodology as the position estimation of a single emitter from a PSF image is the key concept.

18.2.1 Resolution Measures

Which factors then play a role in the resolution of a localization-based image and how can the resolution easily be assessed for experimental data? Already in one of the first key publications by Betzig et al.,[1] it was noted that "both parameters, localization precision and the density of rendered molecules, are key to defining performance." However, it took a few years before this realization was developed further. Initially, researchers simply equated resolution with the average localization uncertainty of the recordings or the average density of localizations. Others showed

full width at half maximum (FWHM) values of cross sections of line-like structures. These concepts will be discussed in the following.

18.2.1.1 Localization Uncertainty

The localization uncertainty indicates the expected standard deviation of the error that was made in estimating a single emitter's position. The localization uncertainty of a single fit to a PSF is only returned by some localization algorithms, mostly those based on maximum-likelihood estimation (MLE) fitting. The uncertainty is then computed using the inverse Fisher matrix,[5,27–31] which gives the theoretically best localization precision that could be achieved. It was shown that fitting with a simple Gaussian PSF model to the data is actually sufficient to achieve the best possible fit in 2D.[32,33] As MLE fitting is in many cases slower than nonlinear least mean squares (LMS) fitting, the latter is very popular and actually quite accurate for a few hundred signal photon counts.

As many algorithms lack the explicit computation of the uncertainty, a very concise and practical formula by Thompson et al. is often used for computing the average localization uncertainty Δx for LMS fitting[34]

$$\left\langle (\Delta x)^2 \right\rangle = \frac{\sigma_a^2}{n}\left(1 + \frac{8\pi\sigma^2 b}{na^2}\right), \tag{18.1}$$

with $\sigma_a^2 = \sigma_{\text{psf}}^2 + a^2/12$. Here, σ_{psf} is the width of the Gaussian that is used to fit the PSF, a is the pixel size, n is the number of signal photons, and b is the number of background photons per pixel. This formula is very widely used in the field as only easily accessible experimental parameters are required to evaluate it. It turned out, however, that it is also unduly optimistic for all cases where the background intensity b is nonzero.[6,7,28] Mortensen et al. presented a formula for the localization uncertainty for MLE fitting:[6]

$$\left\langle (\Delta x)^2 \right\rangle = \frac{\sigma_a^2}{n}\left(1 + \int_0^1 \mathrm{d}t \, \frac{\ln t}{1 + t/\tau}\right)^{-1}, \tag{18.2}$$

where τ is a normalized dimensionless back ground parameter, $\tau = 2\pi\sigma_a^2 b/(na^2)$. This formula can be approximated within a few percent by an analytical expression derived by us earlier:[7]

$$\left\langle (\Delta x)^2 \right\rangle = \frac{\sigma_a^2}{n}\left(1 + 4\tau + \sqrt{\frac{2\tau}{1+4\tau}}\right). \tag{18.3}$$

None of these equations consider the excess noise of the electron multiplication process that is present in the EMCCD (electron-multiplying charge-coupled device) cameras that are normally used for single-molecule imaging.[30] Theoretically, this deteriorates the performance by a factor of $\sqrt{2}$ compared to Equations 18.2 and 18.3.[30] Recently, Huang et al.[35] showed that for this reason, sCMOS (scientific complementary metal oxide semiconductor) cameras outperform EMCCD cameras for

localization microscopy, except in cases with fewer than ~100–200 signal photons per emitter and little background. If only a few photons are detected per pixel on average, EMCCD cameras can be used to achieve the best localization precision.[36]

Even though the Thompson formula is too optimistic for nonzero background intensities, it is still used because of its simplicity. We would recommend using Equation 18.3 instead, as it requires the same input parameters, is simple, and is correct for all cases to within a few percent.

18.2.1.2 Full Width at Half Maximum

Directly related to the localization uncertainty is the FWHM. For a line-like structure with a Gaussian cross section, the relation between its standard deviation σ and the FWHM is $2\sqrt{2\ln 2}\sigma \approx 2.35\sigma$. For a Gaussian distribution of localization errors, the FWHM represents the effective width of the system's PSF. In that sense, stating the FWHM instead of the localization uncertainty provides a fairer comparison to the widefield resolution. A related approach used in all publications by Hell et al. is to indicate the performance of the imaging by extracting line profiles across narrow line-like structures such as tubulin filaments. Also, in localization microscopy, this is a useful measure as it incorporates experimental effects such as the wider appearance of structures owing to the size of the linker plus fluorescent label.[16] The downside of this experimental procedure is that the user must handpick one or more cross sections. This is susceptible to bias toward selecting the best lines instead of representative lines.

18.2.1.3 Two-Point Resolution

The so-called two-point resolution has been defined in the context of localization microscopy by Ram et al.,[37] thus extending the Rayleigh criterion to this imaging modality. Their definition of two-point resolution was the minimal standard deviation with which the distance between two emitters can be estimated. This measure, however, was not used by practitioners in the field as it is not easy to assess this resolution measure by experimentally accessible parameters.

18.2.1.4 Density of Localizations

Another commonly stated quantity intended to indicate the resolution is the density of localizations ρ, which is easily computed directly from the data. It can also be used to compute the two-dimensional (2D) Nyquist random sampling resolution as $2/\sqrt{\rho}$ in 2D or $2\rho^{-1/3}$ in 3D. The Nyquist sampling theorem, however, does not strictly apply since localizations do not constitute samples of a bandwidth-limited function. In addition, a problem that has not received much attention is that individual fluorophores are typically activated and localized several times during an acquisition. The number of times an emitter is reactivated can be quite substantial depending on the imaging and buffer conditions (~5–50 times). Even for imaging with fluorescent proteins, repeated activations have been reported where emitters should have become permanently disabled because of photobleaching.[38,39] If this is the case, then the sampling density is artificially overestimated and, in turn, also the resolution based on the Nyquist density. Nevertheless, the density of localizations is used in the field and describes an additional quality besides the localization uncertainty.

As mentioned above, it has been already realized in 2006 that localization density and uncertainty must both play a role in the resolution;[1] these effects have since been investigated experimentally.[40,41] In the following, we review methods that combine both quantities into one resolution assessment.

18.2.1.5 Kernel Density Estimation

One approach for quantifying the resolution in localization microscopy that takes into account both localization precision and labeling density was proposed by Rees et al.[42] These authors draw on the literature on density estimation and consider filter kernels that provide the best estimation of the fluorophore density of the underlying imaged object. The authors argue that the filtered images show this object blurred first by the localization error and second by the smoothing kernel. The resolution is then defined as the minimal distance for which an intensity minimum can still be seen between two emitters in the filtered image (i.e., the Sparrow resolution criterion). Unfortunately, the determination of the optimal filter kernel size is rather difficult in practice. First, this requires knowledge about the stage drift in the acquisition and the size of the fluorescent labels. Second, the proposed scheme for dealing with variations in the density of localizations is based on statistics of the nearest neighbors of each localization. Since fluorophores are localized an unknown number of times, it is unclear which fluorophores are typically represented by these nearest neighbors. Therefore, rules for determining the kernel size will be susceptible to inconsistent outcomes depending on the statistics of the localizations per fluorophore.

18.2.1.6 Information Transfer Function

The information transfer function[43,44] is a conceptual approach for quantifying resolution that considers the filtering of localization microscopy images in the spatial frequency domain. It describes the theoretically minimal error that can be attained by any linear or nonlinear filtering procedure in estimating the spatial frequency content of the underlying imaged object. The maximum spatial frequency at which this relative error is larger than a certain threshold then defines the resolution of the image. Unfortunately, determining the resolution using this framework requires knowledge of the spatial frequency content of the underlying image structure. It has been suggested that such knowledge may be obtained by using a databank of electron microscopy (EM) images or that the spatial frequency content of the underlying structure can be iteratively estimated.[43] Nevertheless, this requirement severely hinders the practical application of this resolution concept on experimental data.

The above approaches consider the localization uncertainty and density but are not usable in practice and omit the fact that, additionally, the resolution depends on many more factors such as the link between the label and the structure, the underlying spatial structure of the sample itself, and the extensive data processing and visualization required to produce a final super-resolution image. Moreover, these approaches neglect the problems that arise owing to repeated localizations of the same emitter from different activation cycles. This will bias the resolution estimation substantially if not properly taken into account. Therefore, only an integral, image-based resolution measure not depending on a priori information is suitable for determining what level of detail can be reliably discerned in a specific image.

18.2.2 Fourier Ring Correlation

We proposed Fourier ring correlation (FRC) or, equivalently, the spectral signal-to-noise ratio as a practical approach for defining and quantifying resolution in localization microscopy.[45] The FRC is the standard for resolution assessment in the field of cryo-EM single-particle reconstructions of macromolecular complexes.[46–49] In cryo-EM, the resolution is much worse than the diffraction limit given by the electron wavelength and the opening angle, attributed to aberrations in the optical systems. Furthermore, the signal-to-noise ratio is so low (≤1) that the actual image content has to be considered. FRC provides an image-resolution measure that does not require any prior knowledge and is sensitive to the effects of both localization precision and labeling density. Moreover, it is also sensitive to the other factors that influence the resolution mentioned above.

To compute the FRC resolution, the full set of estimated fluorophore positions is divided into two independent subsets. This yields two subimages $f_1(\vec{r})$ and $f_2(\vec{r})$, where $\vec{r}$ denotes the spatial coordinates. Statistical correlation of their Fourier transforms $\hat{f}_1(\vec{q})$ and $\hat{f}_2(\vec{q})$ over the pixels on the perimeter of circles of constant spatial frequency magnitude $q = |\vec{q}|$ then gives the FRC:[47]

$$\mathrm{FRC}(q) = \frac{\sum_{\vec{q}\in\mathrm{circle}} \hat{f}_1(\vec{q})\hat{f}_2(\vec{q})^*}{\sqrt{\sum_{\vec{q}\in\mathrm{circle}} \hat{f}_1(\vec{q})^2}\sqrt{\sum_{\vec{q}\in\mathrm{circle}} \hat{f}_2(\vec{q})^2}}. \tag{18.4}$$

The Fourier transformation of $f(\vec{r})$ is given by $\hat{f}(\vec{q}) = \int d\vec{r} f(\vec{r}) e^{-i2\pi\vec{q}\cdot\vec{r}}$. For low spatial frequencies, the FRC curve is close to unity, and for high spatial frequencies, noise dominates the data and the FRC decays to zero. The image resolution is defined as the inverse of the spatial frequency $R = 1/q_R$ for which the FRC curve drops below a given threshold. See Figure 18.1 for an illustration of the steps needed to compute the FRC resolution. Currently, there is no consensus on what threshold should be used in the field of single-particle EM. Lately, the field does appear to converge on the use of a fixed threshold of 1/7 though.[49,50] We investigated the various threshold criteria empirically[46,50–52] and concluded that the fixed threshold of 1/7 ≈ 0.143 is also the most appropriate one for localization microscopy; that is, $FRC(q_R) = 1/7$.

The expectation of the FRC is given by[45]

$$\left\langle \mathrm{FRC}(q) \right\rangle = \frac{\sum_{\vec{q}\in\mathrm{circle}} \left(Q + N\left|\hat{\psi}(\vec{q})\right|^2\right)\exp\left(-4\pi^2\sigma^2 q^2\right)}{\sum_{\vec{q}\in\mathrm{circle}} \left[2 + \left(Q + N\left|\hat{\psi}(\vec{q})\right|^2\right)\exp\left(-4\pi^2\sigma^2 q^2\right)\right]}, \tag{18.5}$$

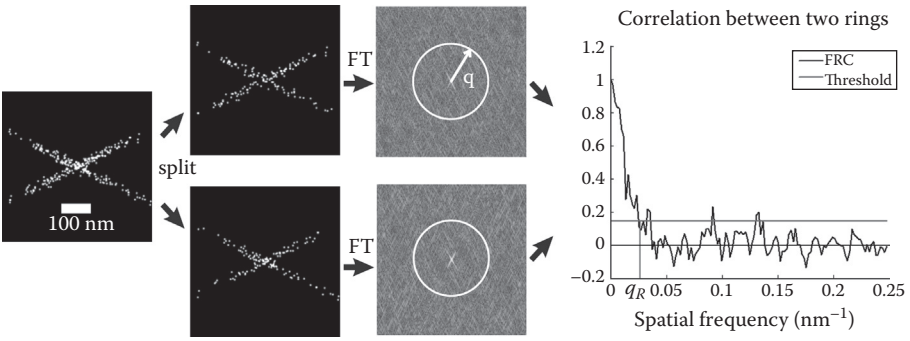

FIGURE 18.1 Schematic illustration of FRC resolution computation. All localizations are divided into two halves, and the correlation of their Fourier transforms over the perimeter of circles in Fourier space of radius q is calculated. This results in an FRC curve indicating the decay of the correlation with spatial frequency. The image resolution is the inverse of the spatial frequency q_R or which the FRC curve drops below the threshold 1/7 ≈ 0.143; thus, for example, $q_R = 0.04$ nm^{-1} is equivalent to 25 nm resolution.

where N is the total number of localized emitters, σ is the average localization uncertainty, and $\hat{\psi}(\vec{q})$ is the Fourier spectrum of the object. The parameter Q takes into account the repeated activation of the same emitter. Each emitter contributing to the image is localized once for $Q = 0$ and in general $Q/(1 - e^{-Q})$ times on average, provided the emitter activation follows Poisson statistics. The term with Q in the numerator of Equation 18.5 is a measure for spurious correlations at high frequencies and can result in overestimation of the resolution. However, this can be corrected for by estimating the parameter Q from the data as explained in Ref. 45. If done so, we have shown that more frequent localization of the same emitter is always beneficial to the final resolution.[53]

For a sample consisting of two parallel lines with a sinusoidal cross section, Equation 18.5 can be solved analytically for $Q = 0$. This results in a resolution $R = 2\pi\sigma \Big/ \sqrt{W(6\pi\rho\sigma^2)}$,[45] where $W(x)$ is the Lambert W-function.[54] This also shows that the localization precision σ and the density of localizations ρ are combined into the FRC resolution estimation in a natural way. More generally, Equation 18.5 shows that the FRC resolution also takes into account the frequency contents of the underlying object without it being known explicitly.

The FRC resolution measure reduces to common resolution measures in limiting cases. In the limit of perfect localization precision, that is, $\sigma \to 0$, the resolution for the two-line sample becomes $R = \sqrt{\pi/6}\ R_{\text{Nyquist}} \approx R_{\text{Nyquist}}$. When the FRC is applied to widefield acquisitions, the resolution reduces to the Abbe resolution in the limit of infinite SNR.[45]

In Section 18.3, the FRC-based resolution approach will be used to evaluate the image resolution attained with various visualization methods for localization microscopy data.

18.2.3 Local and Anisotropic (2D and 3D) Resolution

For experimental images, the apparent resolution is often not homogeneous across the sample, for example, owing to differences in labeling density. In such cases, the FRC resolution and most of the other resolution measures listed above only provide a single number to indicate the smallest details that can be reliably interpreted on average. However, by computing the FRC resolution locally for smaller image patches, it is possible to obtain an indication of the local resolution across the image. This local resolution can be visualized using a false color overlay on the super-resolution image, where the color indicates the local resolution.

Experimental images also often exhibit anisotropy owing to inherent anisotropy in the imaged structure or imaging method. In 2D imaging, this can occur for example if the underlying imaged structure consists of filaments with the same orientation. In three-dimensional imaging, resolution anisotropy often results from anisotropy in the localization precision, which is typically two to three times worse in the axial direction than in the lateral direction.[55–57] For these situations, one would expect that the resolution is also anisotropic, that is, not the same for all directions. Anisotropic image resolution can be described similar to FRC by correlating two images of half the data set in Fourier space over a line in 2D (Fourier line correlation [FLC]) or a plane in 3D (Fourier plane correlation [FPC]) perpendicular to spatial frequency vectors $\vec{q}$. This results in an image with a value for the FLC or FPC for all directions and every spatial frequency magnitude $\|\vec{q}\|$. The resolution can then be assessed by identifying the spatial frequencies where the FLC/FPC is above the threshold.

18.3 VISUALIZATION

Localization microscopy has no natural way to display the recordings. It does not sample the image at pixel locations as in standard widefield microscopy. In widefield microscopy, images are typically recorded on a CCD (charge-coupled device) camera. The pixels of the camera together with the magnification of the objective lens naturally define the way how an image is sampled. The back-projected pixel size is chosen such that it fulfills Nyquist sampling, that is, a pixel should be smaller than half the diffraction limit $d \leq \lambda/(4\mathrm{NA})$, where λ is the wavelength of light and NA is the numerical aperture of the imaging system. The emission photons recorded per CCD pixel bin are translated into analog-to-digital units (ADU) with a linear amplification factor (gain). These ADU are typically discretized into 8-, 12-, or 16-bit integers and they represent the intensity or count values. The recorded sample is therefore visualized as a pixelated image where the discrete intensity scale is about linearly proportional to the recorded number of photons and thus the density of fluorescent molecules. The same natural visualization is shared by confocal microscopy, where the CCD pixel is replaced by a point detection device such as a photomultiplier tube or an avalanche photodiode. The stepping of the scan mirror naturally defines the pixel size. Please note that it is common to have a regular (square) sampling grid of pixels or scan positions, but that is not strictly necessary. To avoid phototoxicity, adaptive schemes of illuminating and recording have been proposed.[58,59]

As localization microscopy lacks any of the above natural ways of visualization, it is an important issue how data should be visualized. Basically, the positions of single fluorescent emitters are estimated from the asynchronous recordings of blinking emitters. To this end, different localization schemes are employed that estimate the positions (i.e., a list of 2D or 3D coordinates), as well as the estimated fluorophore intensities, background intensities, localization precisions, and possibly other parameters depending on the localization method.[5,28,29,31] Thus, localization microscopy produces data sets but no images initially. To make these data comprehensible, these localization data need to be translated into a visual representation in the form of an image. Subsequently, this image needs to be translated into brightness values of the pixels in the display device. Reconstruction (in the Nyquist sense) of the fluorophore distribution of the underlying imaged object from the set of localizations is not considered to be a part of the visualization process.

This section is concerned with the choice of the visualization method for translating localization data into an image. Several methods have been proposed in the literature that will be discussed here: scattergram plots,[3] histogram binning,[13] Gaussian rendering,[1] jittered histogram binning,[60] Delaunay triangulation,[61] and quad-tree visualization.[61]

18.3.1 Description of Visualization Methods

In this subsection, the various visualization methods are first illustrated and described, before moving on to discussing the merits and implications of using the methods in Section 18.3.2. See Figure 18.2 for an illustration of the different visualization methods, except the scattergram method.

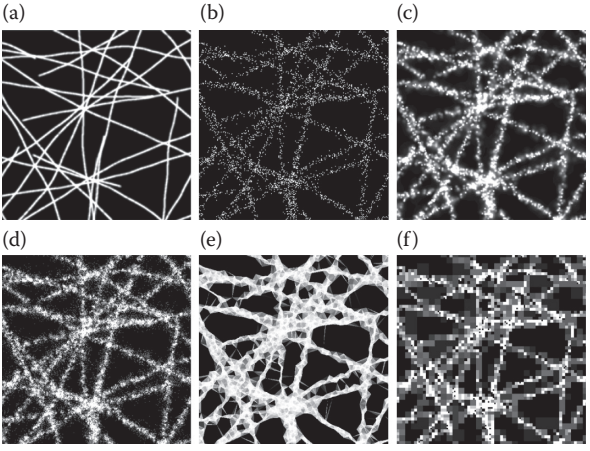

FIGURE 18.2 Illustration of different visualization methods. The images show the different visualization methods applied to simulated localization data of filaments for a density of localizations $\rho = 2.0 \times 10^3\ \mu m^{-2}$ and localization precision $\sigma = 10$ nm. (a) The ground truth structure, (b) histogram binning, (c) Gaussian rendering, (d) jittering, (e) Delaunay triangulation, and (f) quad-tree visualization. Images are individually 95th percentile stretched for better visibility on paper.

Scattergram: Each coordinate is plotted as a symbol, typically a cross or plus, in a Cartesian coordinate system.[3]

Histogram binning: The field of view is divided into a complete set of square pixel bins and the number of localizations that fall in each bin is counted and used to assign intensity values to bins.[13] The size of the pixel bins should generally not exceed one quarter of the image resolution in order not to deteriorate the resolution.[45] Histogram images often appear rather noisy because of the low signal-to-noise ratio per pixel, which can be resolved by postblurring the histogram images. This blurring also prevents problems with aliasing if the sampling density of the display device is too low. If a radially symmetric kernel is used for blurring, then the image resolution remains unchanged for reasonably isotropic structures.[45]

Gaussian rendering: An image is rendered where localizations are represented with Gaussian blobs with a width proportional to the estimated localization precision in the respective axial and lateral dimensions.[1] Thus, the resulting image conveys information on the localization precision of each localization. It should be noted that effects such as imperfect correction for stage drift effectively lead to an additional localization error that is not taken into account in the estimated localization precision. Therefore, the rendered Gaussian blobs cannot always be interpreted to be likelihood functions for the positions of the fluorophores.

Jittered histogram binning: Each localization gives rise to a fixed number of offspring points (typically 10 or 20) that are randomly displaced (i.e., jittered) with a zero-mean normal distribution whose standard deviation is equal to the estimated localization precision.[60] Thus, for very large numbers of offspring points, this visualization method gives the same result as Gaussian rendering.

Delaunay triangulation: A tiling is created in the image plane using triangles whose vertices correspond to the estimated emitter locations.[61] The triangles are rendered with a grayscale intensity inversely proportional to the area of the triangle such that higher local densities of emitters result in higher intensities. The size of the triangles emphasizes the local density of localizations.

Quad-tree visualization: An image is formed using square pixels whose size depends on the local density of localizations.[61] Initially, the image plane is divided into four pixels. Each pixel that contains more than a fixed threshold number of localizations is subsequently split into four subpixels. This process is repeated for the subpixels, until each pixel contains fewer localizations than the threshold value.

18.3.2 Comparison of Visualization Methods

With the multitude of available visualization methods, the question as to which method is best for representing experimental data arises. A number of relevant considerations in choosing a visualization method were discussed by Baddeley et al.[61] Here, we will focus on the most important of those: the extent to which images produced with a visualization method can be intuitively interpreted and the resolution of these images.

Intuitive interpretation of localization microscopy images requires that the images conform to users' expectations based on other fluorescence microscopy methods, such as widefield or confocal imaging. In these microscopy techniques, the local intensity in the image can be described by a convolution of the fluorophore density

in the sample with the effective PSF. Hence, the image intensity values are linear in the density of imaged molecules and typically vary smoothly owing to the effective blurring by the PSF. This linearity is also inherent in super-resolution imaging techniques such as STED,[19,20] SIM,[21,22] and ISM.[23,24]

The expected linearity of intensity values argues against the use of the scattergram visualization method: at a high localization density, the symbols in the scattergram overlap and lead to a saturated image. The Delaunay triangulation and quad-tree methods are also not linear in the density of localized molecules, but these do not provide saturated images.

Linearity is more generally an issue for localization microscopy because the acquisitions are nonlinear in the density of labeled molecules. Some molecules are not localized in an experiment and do not contribute to the final image. Additionally, fluorophore activation events are sometimes not recognized or rejected by the localization software. This could happen, for example, if fluorophores are too dim to be picked up by the algorithm that selects candidates for fitting or too dim to pass the threshold for the allowed localization precision. Also, if nearby fluorophores are simultaneously active such that their emissions overlap in the image plane, then the localization algorithm results in a position intermediate between the two simultaneously active molecules. Although, currently, methods toward multifluorophore fitting[62–64] are proposed, the application of these methods to nonideal acquisitions outside TIRF (total internal reflection fluorescence) imaging remains a challenge. In the worst case, overlapping emissions may result in unnoticed missing structures. Hence, the final images are always nonlinear in the density of labeled molecules. None of the above visualization methods, however, shows activation events missed by the preprocessing software for candidate selection.

The smooth, blurry appearance of images produced with conventional fluorescence microscopy methods normally conveys a sense of the resolution of the imaging system. Therefore, the Gaussian rendering and jittered binning methods vary the apparent width of localizations in images to indicate how well the corresponding fluorophores can be distinguished from nearby molecules. The ability, however, to resolve structures in localization microscopy depends not only on the localization precision but also, for example, on the labeling density.[45] Therefore, the apparent size of localizations in Gaussian rendering and jittered binning methods does not indicate the actual image resolution. Delaunay triangulation and quad-tree visualization emphasize local variations in the image resolution by adjusting the triangle sizes or subpixel sizes to the labeling density. Unfortunately, these sizes do not correspond to the image resolution that would be determined with the FRC method.

18.3.2.1 Simulations

The second consideration for choosing a visualization method that merits attention, next to intuitive interpretation, is the actual image resolution in the image that is produced. This issue will be addressed by studying the resolution of images produced with different visualization methods for simulation data. By using simulation data where the underlying imaged structure is known, it is possible to identify if the FRC between images of two halves of the simulated data is biased. Such a bias could result in inaccurate resolution determination for experimental data.

18.3.2.2 Setup

Localization microscopy acquisitions of filaments were simulated where both the chosen average localization precision σ and density of localizations ρ were varied. For these simulations, the ground truth structure consisted of 100 filaments generated with a worm-like chain model[65–67] for a persistence length of 15 μm (i.e., approximately the persistence length of F-actin[68]). Each filament had a random starting position and starting orientation inside the field of view of 5.12 μm by 5.12 μm. All filaments were then Gaussian blurred with a standard deviation of 5 nm to provide the filaments with a finite width. Subsequently, they were rendered in an image with a pixel size of 2.5 nm.

For this ground truth structure, 100 acquisitions were simulated for each combination of densities ρ and localization uncertainties σ. For each acquisition, a Poisson-distributed number of points was generated with a density proportional to the ground truth structure and average density equal to ρ. These points were then randomly displaced with a Gaussian probability density with variance $d^2 + \sigma_0^2 / n_{\text{photons}}$ to simulate the finite label size and localization error. Here, d represents the finite size of fluorescent labels and had a value $d = 5$ nm. For each point, σ_0 was randomly drawn from a normal distribution with a mean specified by $\langle\sigma_0\rangle = 450$ nm and standard deviation of $0.1 \langle\sigma_0\rangle$. The parameter n_{photons} was randomly drawn from a geometric distribution, which is the distribution for the photon counts of a photon source whose duration has an exponential distribution. These values give a localization uncertainty of 10 nm at 2000 photons.

The simulated localization data were used to compute the resolutions of the images generated by the various visualization methods. For each acquisition, the localizations were split into two half sets to obtain two images per visualization methods. All images had pixel sizes of 5 nm, except the images obtained with Delaunay triangulation, which were rendered using the PALM-siever software[69] with a pixel size of 2.5 nm. For the quad-tree visualization, the threshold number of localization per pixel for splitting into subpixels was 6. Subsequently, the resolution was obtained with these images by computing the FRC and finding the spatial frequency for which the FRC dropped below the threshold of 1/7. To investigate potential biases in the computed FRC curves, additional images were made with all localizations of each acquisition. These were then used to compute the FRC between those images and the ground truth structure. The spatial frequency at which this full data FRC crosses a threshold of 1/2 should give the same result as before for unbiased resolution estimation.[50]

18.3.2.3 Results

The results of the simulations are summarized in Figures 18.3 and 18.4. Figure 18.3 shows the resolution between the full data images and the ground truth structure for the various visualization methods. From this figure, it becomes clear that generally histogram binning, jittering, and Gaussian rendering result in more or less the same resolution. Gaussian rendering provides the best resolution, especially when the mean localization error σ is large and strongly affects the image resolution. This result will be discussed in more detail in the next paragraph. Delaunay triangulation and quad-tree visualization result in substantially deteriorated resolutions when the density ρ is not very high. For Delaunay triangulation, this deterioration is attributed to the hard edges that are introduced. For the quad-tree method, the deterioration is attributed to the lack of shift invariance of the pixel splitting.

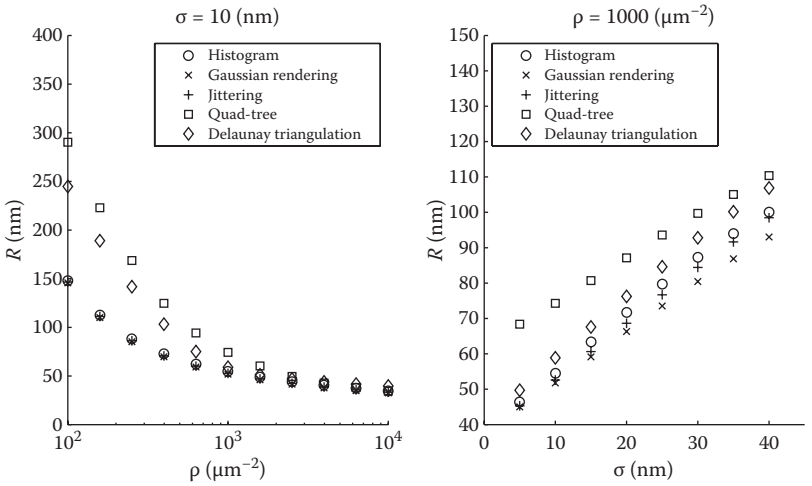

FIGURE 18.3 Resolution for the different visualization methods as a function of the density of localizations ρ and localization precision σ. The resolution is computed from the FRC between images of the full data sets and the ground truth structure. The standard error of the mean is smaller than the marker sizes in this plot.

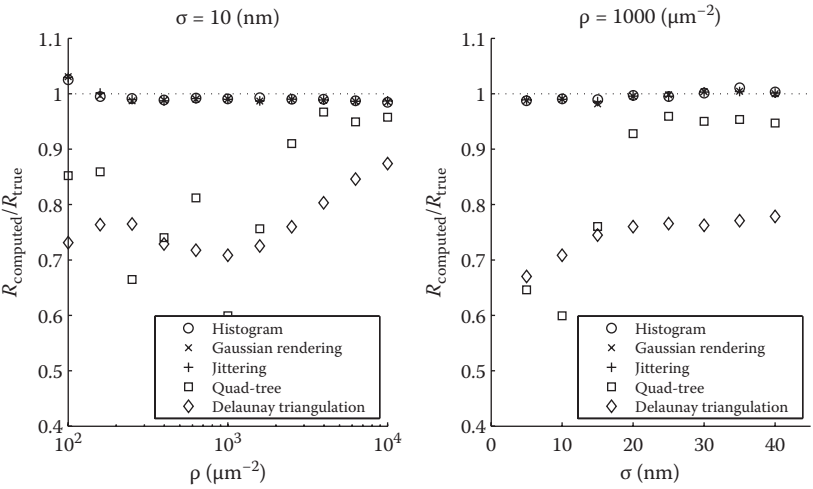

FIGURE 18.4 Bias in resolution estimation for the different visualization methods as a function of the density of localizations ρ and localization precision σ. R_{true} is the resolution obtained from the FRC between images of the full data sets and the ground truth structure, whereas R_{computed} is the resolution obtained from the FRC between two images of half data sets. The standard error of the mean is smaller than the marker sizes in this plot.

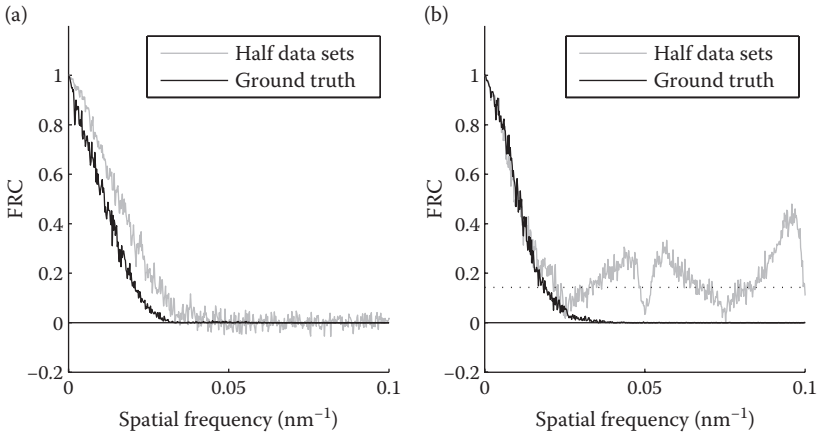

FIGURE 18.5 FRC curves for (a) Delaunay triangulation and (b) quad-tree visualization. The FRC between two images of half data sets is compared here with the curve that would be expected based on the FRC between images of the full data sets and the ground truth structure.

Figure 18.4 shows that Delaunay triangulation and quad-tree visualization bias the resolution estimation with two half data sets for small ρ and small σ. The bias is also evident in Figure 18.5 where the FRC curves between two half data sets are compared with the expected FRC curves based on the FRC between the full data and the ground truth images for these visualization methods. The irregular bias in the quad-tree FRC curve for two half data sets also explains the irregularity in the resolution bias as a function of ρ and σ for that method. All this implies that these visualization methods should not be used to compute and assess the resolution for experimental data.

18.3.2.4 Theoretical Considerations

This section provides a theoretical explanation for why Gaussian rendering performs better than histogram binning. To this end, the expected FRC will be derived for the case where the localization precision σ is not constant for both the Gaussian rendering method and the histogram binning method. Consistent with the simulations above, it will be assumed for simplicity that all fluorophores on the structure at hand are localized exactly once.

Before deriving the expected FRCs, we provide a few definitions. First, the ground truth object for this derivation is given by

$$\psi(\vec{r}) = \sum_{j=1}^{N} \delta\left(\vec{r} - \vec{r}_j^{\,\mathrm{em}}\right), \tag{18.6}$$

where δ is the Dirac delta function. The object depends on the set of positions $\left\{\vec{r}_j^{\,\mathrm{em}} \mid j = 1,\ldots,N\right\}$ of the N fluorophores or labels. These labels are localized at positions $\left\{\vec{r}_j \mid j = 1,\ldots N\right\}$ with probability $P\left(\vec{r}_j\right) = \left(2\pi\sigma_j^2\right)^{-1} \exp\left(-\left\|\vec{r}_j - \vec{r}_j^{\,\mathrm{em}}\right\|^2 \Big/ 2\sigma_j^2\right)$. In the

following, we assume no specific dimensionality, but typically $\vec{r}_j \in \mathbb{R}^2$or $\vec{r}_j \in \mathbb{R}^3$. For the 3D case, the localization uncertainty is typically two to three times worse in the axial direction than in the lateral direction,[55–57] except for very specific experimental setups.[70,71] For the sake of compactness, 2D acquisitions with isotropic localization uncertainties will be assumed, although the conclusions derived here are also valid for anisotropic localization uncertainties.

The set of localizations is split into two subsets of size N_1 and N_2 to produce two images $f_1(\vec{r})$ and $f_2(\vec{r})$, with $N_1 + N_2 = N$ and $N_1 \approx N_2$. The FRC between such images is defined as given by Equation 18.4. The expected value of the numerator of the FRC when emitters are localized is

$$\left\langle \sum_{\vec{q}\in\text{circle}} \hat{f}_1(\vec{q})\hat{f}_2(\vec{q})^* \right\rangle = \sum_{\vec{q}\in\text{circle}} \left\langle \hat{f}_1(\vec{q}) \right\rangle \left\langle \hat{f}_2(\vec{q})^* \right\rangle, \tag{18.7}$$

where $\left\langle f(\vec{r}) \right\rangle \equiv \int \mathrm{d}\vec{r}_1 \ldots \mathrm{d}\vec{r}_N f(\vec{r}) P\left(\left\{\vec{r}_j\right\}\right)$. For Gaussian rendering, the images are denoted by $g_m(\vec{r})$ with $m = \{1, 2\}$, and equal to

$$g_m(\vec{r}) = \sum_{j=1}^{N_m} \frac{1}{2\pi\sigma_j^2} e^{-\left\|\vec{r}-\vec{r}_j\right\|^2 / 2\sigma_j^2}, \tag{18.8}$$

with Fourier transformation

$$\hat{g}_m(\vec{g}) = \sum_{j=1}^{N_m} e^{-2\pi^2 q^2 \sigma_j^2} e^{-i2\pi\vec{q}\cdot\vec{r}j}. \tag{18.9}$$

For the case of constant $\sigma_j \equiv \sigma \forall j$, this expression simply describes a convolution of the found positions r_j with a Gaussian kernel of size σ. Assuming that σ_j is given (i.e., not a stochastic variable), the expected value of $f_m(\vec{q})$ becomes

$$\left\langle \hat{g}_m(\vec{q}) \right\rangle = \int \mathrm{d}\vec{r}_j \sum_{j=1}^{N_m} e^{-2\pi^2 q^2 \sigma_j^2} e^{-i2\pi\vec{q}\cdot\vec{r}_j} P\left(\left\{\vec{r}_j\right\}\right) \tag{18.10}$$

$$= \sum_{j=1}^{N_m} e^{-2\pi^2 q^2 \sigma_j^2} \int \mathrm{d}\vec{r}_j e^{-i2\pi\vec{q}\cdot\vec{r}_j} P\left(\left\{\vec{r}_j\right\}\right) \tag{18.11}$$

$$= \sum_{j=1}^{N_m} e^{-4\pi^2 q^2 \sigma_j^2} e^{-i2\pi\vec{q}\cdot\vec{r}_j^{\text{em}}} \approx \frac{1}{N} \hat{\psi}(\vec{q}) \sum_{j=1}^{N_m} e^{-4\pi^2 q^2 \sigma_j^2}. \tag{18.12}$$

If the effect of low-pass filtering attributed to finite pixel size is neglected, $f_m(\vec{r})$ for histogram binning is equal to

$$f_m(\vec{r}) = \sum_{j=1}^{N_m} \delta\left(\vec{r} - \vec{r}_j\right), \tag{18.13}$$

which leads to

$$\left\langle \hat{f}_m(\vec{q}) \mid \sigma_j \right\rangle \approx \frac{1}{N} \hat{\psi}(\vec{q}) \sum_{j=1}^{N_m} e^{-2\pi^2 q^2 \sigma_j^2}. \tag{18.14}$$

The difference between the two visualization methods already becomes apparent here. Comparing Equations 18.12 and 18.14 show that an extra factor, 2, appears in the exponent because of the extra blurring of the Gaussian rendering. For the expected value of the denominator of the FRC, the expected value of $\left|f_m(\vec{q})\right|^2$ needs to be evaluated. For Gaussian rendering, this goes as follows:

$$\left\langle \left|\hat{g}_m(\vec{q})\right|^2 \right\rangle = \left\langle \sum_{j=1}^{N_m} \sum_{k=1}^{N_m} e^{-2\pi^2 q^2 \sigma_j^2} e^{-2\pi^2 q^2 \sigma_k^2} e^{-i2\pi\vec{q}\cdot\left(\vec{r}_k - \vec{r}_j\right)} \right\rangle \tag{18.15}$$

$$= \left\langle \sum_{j=1}^{N_m} \sum_{k \neq j} e^{-2\pi^2 q^2 \sigma_j^2} e^{-2\pi^2 q^2 \sigma_k^2} e^{-i2\pi\vec{q}\cdot\left(\vec{r}_k - \vec{r}_j\right)} \right\rangle + \left\langle \sum_{j=1}^{N_m} e^{-4\pi^2 q^2 \sigma_j^2} \right\rangle \tag{18.16}$$

$$\approx \left| \left\langle \sum_{j=1}^{N_m} e^{-2\pi^2 q^2 \sigma_j^2} e^{-i2\pi\vec{q}\cdot\vec{r}_j} \right\rangle \right|^2 + \left\langle \sum_{j=1}^{N_m} e^{-4\pi^2 q^2 \sigma_j^2} \right\rangle \tag{18.17}$$

$$= \left| \left\langle \hat{g}_m(\vec{q}) \right\rangle \right|^2 + \left\langle \sum_{j=1}^{N_m} e^{-4\pi^2 q^2 \sigma_j^2} \right\rangle. \tag{18.18}$$

Thus, if the average spectrum of the object over rings of constant spatial frequency is defined as $S(q) = \frac{1}{N^2} \int d^2q' \frac{\delta\left(\left|\vec{q}'\right| - q\right)}{2\pi q} \left|\hat{\psi}(\vec{q}')\right|^2$, the expected FRC becomes

$$\langle \mathrm{FRC} \rangle = \frac{NS(q) \left\langle \exp\left(-4\pi^2 \sigma^2 q^2\right) \right\rangle^2}{2 \left\langle \exp\left(-4\pi^2 \sigma^2 q^2\right) \right\rangle + NS(q) \left\langle \exp\left(-4\pi^2 \sigma^2 q^2\right) \right\rangle^2} \tag{18.19}$$

$$= \frac{NS(q)\left\langle \exp\left(-4\pi^2\sigma^2 q^2\right)\right\rangle}{2 + NS(q)\left\langle \exp\left(-4\pi^2\sigma^2 q^2\right)\right\rangle}. \tag{18.20}$$

Similarly, for histogram binning, the expected value of $\left|f_m(\vec{q})\right|^2$ is

$$\left\langle \left|\hat{f}_m(\vec{q})\right|^2 \right\rangle = \left\langle \sum_{j=1}^{N_m}\sum_{k=1}^{N_m} e^{-i2\pi\vec{q}\left(\vec{r}_k - \vec{r}_j\right)} \right\rangle \approx \left|\left\langle \hat{f}_m(\vec{q})\right\rangle\right|^2 + N_m, \tag{18.21}$$

which leads to the following expected FRC:

$$\langle \mathrm{FRC} \rangle = \frac{NS(q)\left\langle \exp\left(-2\pi^2\sigma^2 q^2\right)\right\rangle^2}{2 + NS(q)\left\langle \exp\left(-2\pi^2\sigma^2 q^2\right)\right\rangle^2}. \tag{18.22}$$

The superiority of the Gaussian rendering over histogram binning now follows from comparing Equations 18.20 and 18.22 and observing that

$$\left\langle e^{-4\pi^2\sigma^2 q^2}\right\rangle - \left\langle e^{-2\pi^2\sigma^2 q^2}\right\rangle^2 = \left\langle \left(e^{-2\pi^2\sigma^2 q^2} - \left\langle e^{-2\pi^2\sigma^2 q^2}\right\rangle\right)^2 \right\rangle \geq 0. \tag{18.23}$$

The explanation for this general superiority on the basis of the equations above is that Gaussian rendering effectively weights the contribution of localizations to spatial frequency components depending on their localization precision. This weighting was already obvious from the comparison of Equations 18.12 and 18.14, which showed that Gaussian rendering introduces an extra factor, 2, in the exponent. This causes the exponentials corresponding to imprecise localizations to decrease faster, and therefore, those localizations contribute less to high-frequency components. This leads to higher correlations at those frequencies. For a constant localization uncertainty for all localizations, that is, $\sigma_j \equiv \sigma \forall j$, both visualization methods are equivalent as the difference in Equation 18.23 is then equal to zero.

This derivation did not include the effects of finite pixel size and multiple localizations per emitter. Low-pass filtering attributed to finite pixel sizes introduces an extra damping of $S(q)$, which is the same for histogram binning and Gaussian rendering. For very large pixel sizes, the damping owing to finite pixel size will be stronger than damping owing to the localization error, thus negating the benefits of Gaussian rendering. For multiple localizations per emitter, the impact of Gaussian rendering on the FRC is more subtle and dependent on the statistics of the localization uncertainties σ_j.

18.4 DISCUSSION AND CONCLUSION

The above results lead to the conclusion that the Gaussian rendering method provides the best resolution of the evaluated visualization methods. Please note that this is only true if the Gaussian blobs reflect the localization uncertainty of each single fluorophore and not if one applies one global Gaussian kernel to all localizations. Since this method is also linear in the density of localizations and conveys information about the localization precision, it seems to be the visualization method of choice. However, the histogram binning method provides a similar resolution in a shorter computation time and is therefore a good alternative method. In particular, the reduced computation time makes histogram binning the preferred method for fast and unbiased resolution determination. When this method is used for visualization, it is recommended to postblur the image, for example, with a Gaussian kernel with a standard deviation equal to the average localization precision. This reduces the noise in the image without reducing the resolution. The jittering method provides a compromise between the histogram binning and Gaussian rendering methods, with a better resolution than histogram binning and typically a shorter computation time than Gaussian rendering. Quad-tree visualization and Delaunay triangulation lead to resolution deterioration and biased resolution estimation and are therefore not recommended.

A significant limitation of this simulation study is that the ground truth structure and the Delaunay triangulation results had to be pixelated to compute their Fourier transforms, even though they contain infinitely high spatial frequency components. In principle, this could lead to changes in frequency contents caused by aliasing and the effective low-pass filtering attributed to the finite pixel size. The resolutions, however, in these simulations were typically more than 20 times the pixel size of these images. Therefore, these problems should not play a role at the spatial frequencies where the FRC drops below the threshold and should not affect the computed resolution.

REFERENCES

1. Betzig, E., G. Patterson, R. Sougrat, O. Lindwasser, S. Olenych, J. Bonifacino, M. Davidson, J. Lippincott-Schwartz, and H. Hess. “Imaging intracellular fluorescent proteins at nanometer resolution.” *Science 313* (2006): 1643–5.
2. Hess, S., T. Girirajan, and M. Mason. “Ultra-high resolution imaging by fluorescence photoactivation localization microscopy.” *Biophysical Journal 91* no. 11 (2006): 4258–72.
3. Rust, M., M. Bates, and X. Zhuang. “Sub-diffraction-limit imaging by stochastic optical reconstruction microscopy (STORM).” *Nature Methods 3* no. 10 (2006): 793–5.
4. Ober, R., Z. Lin, and Q. Zou. “Calculations of the fisher information matrix for multidimensional data sets.” *IEEE Transactions on Signal Processing 51* no. 10 (2003): 2679–91.
5. Ober, R., S. Ram, and S. Ward. “Localization accuracy in single-molecule microscopy.” *Biophysical Journal 86* no. 2 (2004): 1185–200.
6. Mortensen, K., L. Churchman, J. Spudich, and H. Flyvbjerg. “Optimized localization analysis for single-molecule tracking and super-resolution microscopy.” *Nature Methods 7* no. 5 (2010): 377–84.

7. Stallinga, S. and B. Rieger (2012). "The effect of background on localization uncertainty in single emitter imaging." In *IEEE International Symposium on Biomedical Imaging*, Barcelona, Spain, pp. 988–91.
8. Pertsinidis, A., Y. Zhang, and S. Chu. "Subnanometre single-molecule localization, registration and distance measurements." *Nature 466* (2010): 647–51.
9. Vaughan, J., S. Jia, and X. Zhuang. "Ultrabright photoactivatable fluorophores created by reductive caging." *Nature Methods 9* no. 12 (2012): 1181–4.
10. Xu, K., G. Zhong, and X. Zhuang. "Actin, spectrin, and associated proteins form a periodic cytoskeletal structure in axons." *Science 339* (2013): 452–6.
11. Hofmann, M., C. Eggeling, S. Jakobs, and S. Hell. "Breaking the diffraction barrier in fluorescence microscopy at low light intensities by using reversibly photoswitchable proteins." *Proceedings of the National Academy of Sciences USA 102* no. 49 (2005): 17565–9.
12. Bock, H., C. Geisler, C. A. Wurm, C. V. Middendorff, S. Jakobs, A. Schönle, A. Egner, S. W. Hell, and C. Eggeling. "Two-color far-field fluorescence nanoscopy based on photoswitchable emitters." *Applied Physics B—Lasers and Optics 88* no. 2 (2007): 161–5.
13. Egner, A., C. Geisler, C. V. Middendorff, H. Bock, D. Wenzel, R. Medda, M. Andresen, A. Stiel, S. Jakobs, C. Eggeling, A. Schönle, and S. Hell. "Fluorescence nanoscopy in whole cells by asynchronous localization of photoswitching emitters." *Biophysical Journal 93* no. 9 (2007): 3285–90.
14. Bates, M., B. Huang, G. T. Dempsey, and X. Zhuang. "Multicolor super-resolution imaging with photo-switchable fluorescent probes." *Science 317* no. 5845 (2007): 1749–53.
15. Heilemann, M., S. V. d. Linde, M. Schüttpelz, R. Kasper, B. Seefeldt, A. Mukherjee, P. Tinnefeld, and M. Sauer. "Subdiffraction-resolution fluorescence imaging with conventional fluorescent probes." *Angewandte Chemie 47* no. 33 (2008): 6172–76.
16. Ries, J., C. Kaplan, E. Platonova, H. Eghlidi, and H. Ewers. "A simple, versatile method for GFP-based super-resolution microscopy via nanobodies." *Nature Methods 9* no. 6 (2012): 582–7.
17. Fölling, J., M. Bossi, H. Bock, R. Medda, C. Wurm, B. Hein, S. Jacobs, C. Eggeling, and S. Hell. "Fluorescence nanoscopy by ground-state depletion and single-molecule return." *Nature Methods 5* (2008): 943–5.
18. Grotjohann, T., T. Testa, M. Leutenegger, H. Bock, N. Urban, F. Lavoie-Cardinal, K. Willig, C. Eggeling, and S. Hell. "Diffraction-unlimited all-optical imaging and writing with a photochromic GFP." *Nature 478* (2011): 204–8.
19. Hell, S. and J. Wichmann. "Breaking the diffraction limit resolution by stimulated emission: Stimulated-emission-depletion microscopy." *Optics Letters 19* no. 11 (1994): 780–3.
20. Hell, S. "Far-field optical nanoscopy." *Science 316* (2007): 1153–8.
21. Gustafsson, M. "Surpassing the lateral resolution limit by a factor of two using structured illumination microscopy." *Journal of Microscopy 198* no. 2 (2000): 82–7.
22. Heintzmann, R. and M. Gustafsson. "Subdiffraction resolution in continuous samples." *Nature Photonics 3* (2009): 362–4.
23. Sheppard, C. "Super-resolution in confocal microscopy." *Optik 80* no. 2 (1988): 53–4.
24. Müller, C. and J. Enderlein. "Image scanning microscopy." *Physical Review Letters 104* (2010): 198101.
25. Abbe, E. "Beiträge zur Theorie des Mikroskopes und der mikroskopischen Wahrnehmung." *Archiv für Mikroskopische Anatomie 9* (1873): 413–68.
26. Nyquist, H. "Certain topics in telegraph transmission theory." *Transactions of the AIEE 90* (1928): 617–44. (reprinted in: *Proceedings of the IEEE 90* no. 2 [2002]: 280–305).
27. Aguet, F., D. V. D. Ville, and M. Unser. "Dynamic multiple-target tracing to probe spatiotemporal cartography of cell membranes." *Optics Express 13* no. 26 (2005): 10503–22.

28. Smith, C., N. Joseph, B. Rieger, and K. Lidke. "Fast, single-molecule localization that achieves theoretically minimum uncertainty." *Nature Methods 7* no. 5 (2010): 373–5.
29. Abraham, A., S. Ram, J. Chao, E. Ward, and R. Ober. "Quantitative study of single molecule location estimation techniques." *Optics Express 17* no. 26 (2009): 23352–73.
30. Chao, J., E. Ward, and R. Ober. "Fisher information matrix for branching processes with application to electron-multiplying charge-coupled devices." *Multidimensional System and Signal Processing 23* (2012): 349–79.
31. Wolter, S., A. Löschberger, T. Holm, S. Aufmkolk, M.-C. Dabauvalle, S. V. D. Linde, and M. Sauer. "rapidSTORM: Accurate, fast open-source software for localization microscopy." *Nature Methods 9* no. 11 (2012): 1040–1.
32. Zhang, B., J. Zerubia, and J.-C. Olivio-Marin. "Gaussian approximations of fluorescence microscope point-spread function models." *Applied Optics 46* no. 10 (2007): 1819–29.
33. Stallinga, S. and B. Rieger. "Accuracy of the Gaussian point spread function model in 2D localization microscopy." *Optics Express 18* no. 24 (2010): 24461–76.
34. Thompson, R., D. Larson, and W. Webb. "Precise nanometer localization analysis for individual fluorescent probes." *Biophysical Journal 82* (2002): 2775–83.
35. Huang, F., T. Hartwich, F. Rivera-Molina, Y. Lin, C. Whitney, J. Long, P. Uchil, J. Myers, M. Baird, W. Mothes, M. Davidson, D. Toomre, and J. Bewersdorf. "Video-rate nanoscopy using sCMOS camera-specific single-molecule localization algorithms." *Nature Methods 10* no. 7 (2013): 653–8.
36. Chao, J., S. Ram, E. Ward, and R. Ober. "Ultrahigh accuracy imaging modality for super-localization microscopy." *Nature Methods 10* (2013): 335–8.
37. Ram, S., E. Ward, and R. Ober. "Beyond Rayleighs criterion: A resolution measure with application to single-molecule microscopy." *Proceedings of the National Academy of Sciences USA 103* no. 12 (2006): 4457–62.
38. Annibale, P., S. Vanni, M. Scarselli, U. Rothlisberger, and A. Radenovic. "Quantitative photo activated localization microscopy: Unraveling the effects of photoblinking." *PLoS ONE 6* no. 7 (2011): e22678.
39. Annibale, P., S. Vanni, M. Scarelli, U. Rothlisberger, and A. Radenovic. "Identification of clustering artifacts in photoactivated localization microscopy." *Nature Methods 8* no. 7 (2011): 527–8.
40. Linde, S. V. D., S. Wolter, M. Heilemann, and M. Sauer. "The effect of photoswitching kinetics and labeling densities on super-resolution fluorescence imaging." *Journal of Biotechnology 149* (2010): 260–6.
41. Cordes, T., J. Vogelsang, M. Anaya, C. Spaguolo, A. Gietl, W. Summerer, A. Herrmann, K. Müllen, and P. Tinnefeld. "Single-molecule redox blinking of perylene diimide derivatives in water." *Journal of the American Chemical Society 132* no. 7 (2010): 2404–9.
42. Rees, E., M. Erdelyi, D. Pinotsi, A. Knight, D. Metcalf, and C. Kaminski. "Blind assessment of localization microscope image resolution." *Optical Nanoscopy 1* (2012): 12.
43. Fitzgerald, J., J. Lu, and M. Schnitzer. "Estimation theoretic measure of resolution for stochastic localization microscopy." *Physical Review Letters 109* (2012): 048102.
44. Mukamel, E. and M. Schnitzer. "Unified resolution bounds for conventional and stochastic localization fluorescence microscopy." *Physical Review Letters 109* (2012): 168102.
45. Nieuwenhuizen, R., K. Lidke, M. Bates, D. Leyton Puig, D. Grünwald, S. Stallinga, and B. Rieger. "Measuring image resolution in optical nanoscopy." *Nature Methods 10* (2013): 557–62.
46. Saxton, W. and W. Baumeister. "The correlation averaging of a regularly arranged bacterial cell envelope protein." *Journal of Microscopy 127* no. 2 (1982): 127–38.
47. Heel, M. V. "Similarity measures between images." *Ultramicroscopy 21* (1987): 95–100.
48. Unser, M., B. Trus, and A. Steven. "A new resolution criterion based on spectral signal-to-noise ratio." *Ultramicroscopy 23* (1987): 39–52.

49. Scheres, S. and S. Chen. "Prevention of overfitting in cryo-em structure determination." *Nature Methods 9* no. 9 (2012): 853–4.
50. Rosenthal, P. and R. Henderson. "Optimal determination of particle orientation, absolute hand, and contrast loss in single-particle electron cryomicroscopy." *Journal of Molecular Biology 333* no. 4 (2003): 721–45.
51. Beckmann, R., D. Bubeck, R. Grassucci, P. Penczek, A. Verschoor, G. Blobel, and J. Frank. "Alignment of conduits for the nascent polypeptide chain in the ribosome–sec61 complex." *Science 278* no. 5346 (1997): 213–6.
52. Böttcher, B., S. Wynne, and R. Crowther. "Determination of the fold of the core protein of hepatitis B virus by electron cryomicroscopy." *Nature 386* no. 6620 (1997): 88–91.
53. Nieuwenhuizen, R., S. Stallinga, and B. Rieger (2013, August 26–30). "Image resolution in optical nanoscopy." In P. Verma and A. Egner (Eds.), *Nanoimaging and Nanospectroscopy*, SPIE Conference vol. 8815, San Diego, USA, p. 881508.
54. Barry, D., J.-Y. Parlange, L. Li, H. Prommer, C. Cunningham, and F. Stagnitti. "Analytical approximations for real values of the Lambert W-function." *Mathematics and Computers in Simulation 53* no. 1–2 (2000): 95–103.
55. Holtzer, L., T. Meckel, and T. Schmidt. "Nanometric three-dimensional tracking of individual quantum dots in cells." *Applied Physics Letters 90* (2007): 053902.
56. Pavani, S. and R. Piestun. "Three dimensional tracking of fluorescent microparticles using a photon-limited double-helix response system." *Optics Express 16* no. 26 (2008): 22048–57.
57. Toprak, E., J. Enderlein, S. Syed, S. McKinney, R. Petschek, T. Ha, Y. Goldman, and P. Selvin. "Defocused orientation and position imaging (DOPI) of myosin V." *Proceedings of the National Academy of Sciences USA 103* no. 17 (2006): 6495–9.
58. Hoebe, R., C. V. Oven, T. J. Gadella, P. Dhonukshe, C. V. Noorden, and E. Manders. "Controlled light-exposure microscopy reduces photobleaching and phototoxicity in fluorescence live-cell imaging." *Nature Biotechnology 25* no. 2 (2007): 249–53.
59. Caarls, W., B. Rieger, A. D. Vries, D. Arndt-Jovin, and T. Jovin. "Minimizing light exposure with the programmable array microscope." *Journal of Microscopy 241* no. 1 (2011): 101–10.
60. Krizek, P., I. Raska, and G. Hagen. "Minimizing detection errors in single molecule localization microscopy." *Optics Express 19* no. 4 (2011): 3226–35.
61. Baddeley, D., M. Cannell, and C. Soeller. "Visualization of localization microscopy data." *Microscopy and Microanalysis 16* (2010): 64–72.
62. Holden, S., S. Uphoff, and A. Kapanidis. "DAOSTORM: An algorithm for high-density super-resolution microscopy." *Nature Methods 8* no. 4 (2011) 279–80.
63. Huang, F., S. Schwartz, J. Byars, and K. Lidke. "Simultaneous multiple-emitter fitting for single molecule super-resolution imaging." *Biomedical Optics Express 2* no. 5 (2011): 1377–93.
64. Zhu, L., W. Zhang, D. Elnatan, and B. Huang. "Faster STORM using compressed sensing." *Nature Methods 9* no. 7 (2012): 721–6.
65. Kratky, O. and G. Porod. "Röntgenuntersuchungen gelöster Fadenmoleküle." *Recueil des Travaux Chimies des Pays-Bas 68* (1949): 1106–24.
66. Landau, L. and E. Lifshitz (1969). *Statistical Physics, Part 1*, second ed. Oxford: Pergamon Press.
67. Faas, F., B. Rieger, L. V. Vliet, and D. Cherny. "DNA deformations near charged surfaces: Electron and atomic force microscopy views." *Biophysical Journal 97* no. 4 (2009): 1148–57.
68. Gittes, F., J. Mickey, B. Nettleton, and J. Howard. "Flexural rigidity of microtubules and actin filaments measured from thermal fluctuations in shape." *Journal of Cell Biology 120* no. 4 (1993): 923–34.

69. Pengo, T. (2013). "PALM-siever: Visualization and analysis platform for single-molecule localization microscopy." Available at http://www.code.google.com/p/palm-siever (accessed September 12, 2013).
70. Middendorff, C. V., A. Egner, C. Geisler, S. Hell, and A. Schönle. "Isotropic 3D nanoscopy based on single emitter switching." *Optics Express 16* no. 25 (2008): 20774–88.
71. Shtengel, G., J. Galbraith, C. Galbraith, J. Lippincott-Schwartz, J. Gillette, S. Manely, R. Sougrat, C. Waterman, P. Knachanawong, M. Davidson, R. Fetter, and H. Hess. "Interferometric fluorescent super-resolution microscopy resolves 3D cellular ultrastructure." *Proceeding of the National Academy of Science USA 106* no. 9 (2009): 3125–30.